Symmetry-enforced band crossings in trigonal materials: Accordion states and Weyl nodal lines

Y.-H. Chan,[1,2,*] Berkay Kilic,[3,4] Moritz M. Hirschmann,[3] Ching-Kai Chiu,[5] Leslie M. Schoop,[6] Darshan G. Joshi,[3] and Andreas P. Schnyder[3,†]

[1]*Institute of Atomic and Molecular Sciences, Academia Sinica, Taipei 10617, Taiwan*
[2]*Materials Sciences Division, Lawrence Berkeley National Laboratory, Berkeley, California 94720, USA*
[3]*Max-Planck-Institut für Festkörperforschung, Heisenbergstrasse 1, D-70569 Stuttgart, Germany*
[4]*Institute for Functional Materials and Quantum Technologies, University of Stuttgart, Pfaffenwaldring 57, D-70550 Stuttgart, Germany*
[5]*Kavli Institute for Theoretical Sciences, University of Chinese Academy of Sciences, Beijing 100190, China*
[6]*Department of Chemistry, Princeton University, Princeton, New Jersey 08544, USA*

(Received 12 August 2019; revised manuscript received 7 November 2019; published 23 December 2019)

Nonsymmorphic symmetries, such as screw rotations or glide reflections, can enforce band crossings within high-symmetry lines or planes of the Brillouin zone. When these band degeneracies are close to the Fermi energy, they can give rise to a number of unusual phenomena, e.g., anomalous magnetoelectric responses, transverse Hall currents, and exotic surface states. In this paper, we present a comprehensive classification of such nonsymmorphic band crossings in trigonal materials with strong spin-orbit coupling. We find that in trigonal systems there are two different types of nonsymmorphic band degeneracies: (i) Weyl points protected by screw rotations with an accordion-like dispersion, and (ii) Weyl nodal lines protected by glide reflections. We report a number of existing materials, where these band crossings are realized near the Fermi energy. This includes Cu_2SrSnS_4 and elemental tellurium (Te), which exhibit accordion Weyl points, and the tellurium-silicon clathrate $Te_{16}Si_{38}$, which shows Weyl nodal lines. The *ab initio* band structures and surface states of these materials are studied in detail, and implications for experiments are briefly discussed.

DOI: 10.1103/PhysRevMaterials.3.124204

I. INTRODUCTION

When two Bloch bands of the same symmetry approach each other at a generic momentum, they generally start to hybridize and undergo an avoided level crossing. This is because band crossings [1] are generally stable only in the presence of symmetry constraints, with the notable exception of Weyl points.

The stability of (symmetry-protected) band crossings is guaranteed by nontrivial wave function topologies [2–6]. When these band crossings are in the vicinity of the Fermi energy, they lead to a range of interesting phenomena, such as arc and drumhead surface states [7–13], transverse topological currents [4,5,14], and anomalous magnetoelectric responses [15], which could potentially be utilized for device applications [16,17].

There are two different types of topological band crossings, namely, accidental band crossings and symmetry-enforced band crossings. The former can be protected by symmorphic crystal symmetries and are only perturbatively stable [18–20]. That is, they can be adiabatically removed by large symmetry-preserving deformations of the Hamiltonian, for example, through pair annihilation. Examples of accidental band crossings include Dirac points and Dirac lines that are protected by space-time inversion, reflection, or rotation symmetry [21–26]. Another example is Weyl points which can be stable even in the absence of symmetries [4]. Symmetry-enforced band crossings [15,27–39], on the other hand, arise in the presence of *nonsymmorphic* symmetries and are globally stable; i.e., they cannot be removed even by large deformations of the Hamiltonian. In other words, these band crossings are required to exist due to nonsymmorphic symmetries alone, independent of the chemical composition and other details of the material. This fact allows us to construct the following strategy to discover new topological semimetals, which consists of three steps: (i) identify the space groups (SGs) whose nonsymmorphic symmetries enforce the desired band crossings, (ii) perform a database search for materials in these SGs, and (iii) compute the electronic band structure of these materials to check whether the band crossings are near the Fermi energy. Previously, we applied this strategy to discover new topological semimetals with hexagonal symmetries [39]. Here, we extend this analysis to trigonal systems.

There have been a number of previous works that considered specific types of nonsymmorphic band crossings [15,33–36] and proposed candidate materials, where these are realized [40–43]. However, a comprehensive classification of all possible nonsymmorphic band crossings in trigonal materials has not been performed before. We find that among the 25 trigonal SGs, six support Weyl points with accordion-like dispersions and three support Weyl nodal lines (see Table I). We identify several materials where these topological band crossings are realized. This includes elemental tellurium (Te) with accordion Weyl points, and the trigonal high-temperature form of $Te_{16}Si_{38}$ with Weyl nodal lines. As a by-product of our analysis, we also obtain the tight filling constraints for the

*yanghao@umich.edu
†a.schnyder@fkf.mpg.de

TABLE I. Classification of nonsymmorphic band crossings in trigonal materials with time-reversal symmetry and strong spin-orbit coupling. The first column lists the trigonal space groups that exhibit topological band crossings. The second and third columns indicate the high-symmetry lines and planes in which Weyl nodal points and Weyl nodal lines appear, respectively. The definition of the coordinate system and high-symmetry labels in the Brillouin zones are given in Figs. 1(a) and 3. The electron fillings ν for which a band insulator is possible are given in the fourth column, where $m\mathbb{N}$ denotes the set $\{m, 2m, 3m, \ldots\}$. Example materials which realize the predicted band crossings are listed in the last column.

Space group	Weyl nodal points	Weyl nodal lines	Filling constraint	Materials
144 ($P3_1$)	$\Gamma\Delta A$ (6)		$6\mathbb{N}$	Cu_2SrSnS_4
145 ($P3_2$)	$\Gamma\Delta A$ (6)		$6\mathbb{N}$	Cu_2SrGeS_4
151 ($P3_112$)	$\Gamma\Delta A$ (6)		$6\mathbb{N}$	Ag_2HPO_4
152 ($P3_121$)	$\Gamma\Delta A$ (6)		$6\mathbb{N}$	Te, Se
153 ($P3_212$)	$\Gamma\Delta A$ (6)		$6\mathbb{N}$	
154 ($P3_221$)	$\Gamma\Delta A$ (6)		$6\mathbb{N}$	
158 ($P3c1$)		k_xk_z plane	$4\mathbb{N}$	
159 ($P31c$)		$k_x = \pi$	$4\mathbb{N}$	
161 ($R3c$)		$k_x = -k_y$	$4\mathbb{N}$	$Te_{16}Si_{38}$

existence of band insulators, which are in agreement with the recent literature [44,45]. Furthermore, we find that in trigonal materials, as opposed to hexagonal materials [39], there exist no band crossings protected by off-centered symmetries [35,37,38]. We note that our analysis takes into account the full connectivity of the bands in the entire Brillouin zone (BZ), which goes beyond the results obtained through symmetry indicators [46–48].

The remainder of this paper is organized as follows. In Sec. II we classify Weyl points protected by screw-rotation symmetries and discuss how symmetries constrain the multiplicities of the Weyl points. Section III is devoted to the study of Weyl nodal lines protected by glide reflection. In Sec. IV we discuss the filling constraints imposed by the nonsymmorphic symmetries. In Sec. V we present the example materials that realize the predicted band crossings. Our summary and conclusions are given in Sec. VI. In Appendix A we present additional figures of the band structure calculations. The calculated surface states of tellurium are shown in Appendix B.

II. NONSYMMORPHIC NODAL POINTS

In this section we show how threefold screw-rotation symmetries in trigonal space groups lead to protected Weyl points. To derive this we employ two different approaches: (i) Using symmetry analysis we show how the evolution of eigenvalues of the symmetry operator along a line in the BZ enforces band crossings (Sec. II A). (ii) Using crystallographic group theory we show how the compatibility relations between irreducible representations (irreps) at different high-symmetry points of the BZ [49–51] lead to enforced band crossings (Sec. II B). We also give a brief discussion on how time-reversal and SG symmetries lead to higher multiplicities of the Weyl points (Sec. II C).

A. Symmetry eigenvalues

In general, a symmetry operator $G = \{g|\vec{t}\}$ of a given space group is a combination of a point group symmetry g and a lattice translation $\vec{t}$. In the case of a nonsymmorphic symmetry the lattice translation $\vec{t}$ is some fraction of the Bravais lattice vector. Here, we are interested in the threefold screw rotation, which has the following form:

$$C_{3,p} : (x, y, z) \to \left(-y, x - y, z + \frac{p}{3}\right) \otimes \left(\frac{1}{2}\sigma_0 - \frac{i\sqrt{3}}{2}\sigma_z\right), \tag{2.1}$$

such that $p \in \{1, 2\}$. Here, the three-component vectors indicate how the screw rotation transforms the numerical coordinates in a trigonal coordinate system. The second bracket on the right-hand side specifies how the electronic spin is transformed by the screw rotation. Within the g-invariant space of the BZ, i.e., where $g\vec{k} = \vec{k}$, the Bloch states $|\psi_m(\vec{k})\rangle$ can be constructed to be simultaneous eigenfunctions of G and the Hamiltonian, satisfying the following eigenvalue equation:

$$C_{3,p}|\psi_m(\vec{k})\rangle = e^{i\pi(2m+1)/3}e^{-ipk_z/3}|\psi_m(\vec{k})\rangle, \tag{2.2}$$

with $m \in \{0, 1, 2\}$. The above equation follows from the fact that $C_{3,p}^3 = -p\vec{R}$, where $\vec{R}$ is a Bravais lattice vector (here $\vec{R} = \hat{z}$) and the minus sign arises due to 2π rotation of the electron spin, relevant for spin-orbit coupling. From Eq. (2.2), we observe that the eigenvalues of $C_{3,p}$ evolve along the line segment $\vec{k} = (0, 0, k_z)$ with $k_z \in [0, \pi]$, i.e., along the path Γ-Δ-A in Fig. 1, which is invariant under C_3 rotation.

Note that the points Γ and A are time-reversal invariant momenta, where in the presence of time-reversal symmetry

TABLE II. This table lists how the Bloch bands $|\psi_m(\vec{k})\rangle$ pair up into Kramers partners at the A point of the BZ in materials with a threefold screw rotation $C_{3,p}$. The pairing depends on p, i.e., the fractional lattice translation part of $C_{3,p}$; see Eq. (2.2). The right column indicates the eigenvalue labels m of the Kramers pairs at the A point.

p	Pairings of m
1	(0,0), (1,2)
2	(0,1), (2,2)

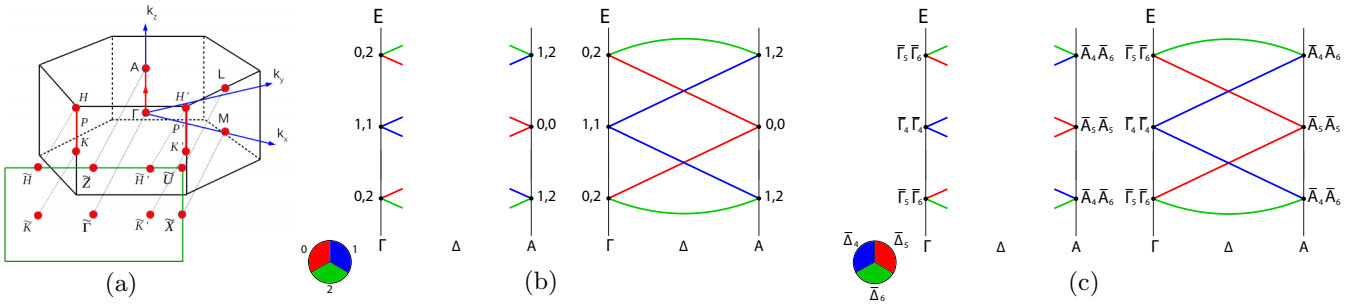

FIG. 1. (a) Bulk BZ (black lines) for trigonal space groups with hexagonal lattice systems (*P*-trigonal). The high-symmetry points and lines are indicated in red. The green lines show the surface BZ for surfaces perpendicular to the (-110) direction. (b), (c) Kramers pairings and band connectivity diagrams for the Γ-Δ-*A* line of the hexagonal BZ, which is left invariant by the threefold screw rotation $C_{3,p}$. Here, we focus on the case $p = 1$, e.g., on SG No. 144 ($P3_1$). (Similar band crossings are also realized for $p = 2$.) The left panels in (b) and (c) indicate how the Bloch bands $|\psi_m(\vec{k})\rangle$ pair up into Kramers partners at the time-reversal invariant momenta Γ and *A*; see Tables II and III. The right panels in (b) and (c) show the band connectivity diagrams along the path Γ-Δ-*A*. Six bands form a connected group with at least two symmetry-enforced Weyl points, as explained in the text. In (b) the bands are marked by their $C_{3,p}$ eigenvalue label *m*, while in (c) they are marked by their double-valued irreps $\bar{\Delta}_i$.

bands pair up with their respective Kramers partner. In terms of the eigenvalues in Eq. (2.2) this means that a band with a real eigenvalue pairs with itself, while a band with a complex eigenvalue pairs with the band whose eigenvalue is the complex conjugate. Using the label *m* to identify the bands and corresponding eigenvalues, we find the following pairing scenario: At the Γ point ($k_z = 0$) there are two Kramers pairs of bands, namely, (1,1) and (0,2), irrespective of the value of *p*. At the *A* point ($k_z = \pi$), on the other hand, Kramers pairs depend on the value of *p* and pair up as indicated in Table II. Since the bands pair up differently at Γ and *A*, they show, in the absence of additional symmetries, a nontrivial connectivity along the path Γ-Δ-*A*, as displayed in Fig. 1(b). We find that for both $p = 1$ and $p = 2$ there are six bands forming a connected group, which must cross at least two times, leading to two Weyl point degeneracies. Since the dispersion of this group of six bands is reminiscent of an accordion, we call it an "accordion dispersion" [39]. In the following we will use the term "accordion states" to refer to a group of $2k$ connected bands (with $k > 2$) along a high-symmetry line (or high-symmetry plane) which cross at least $k - 1$ times. An example of this for $k = 3$ is shown in Fig. 1(b). When $k = 2$ the group of four connected bands is called an "hourglass state" [32]; see Fig. 3(a).

We note that the presence of additional symmetries, such as inversion or mirror, which either commute or anticommute with $C_{3,p}$, may lead to additional degeneracies at the high-symmetry points in the BZ. This can remove the above discussed Weyl points. In particular, out of the 18 trigonal space groups with a hexagonal lattice system (*P*-trigonal) there are only six space groups without inversion symmetry (SGs with Nos. 144, 145, 151, 152, 153, and 154). These are the only SGs which host symmetry-enforced Weyl points with accordion-like dispersions; see Table I.

In passing we note that the seven trigonal space groups with rhombohedral lattice system (*R*-trigonal) do not have a nonsymmorphic threefold screw-rotation symmetry, but just threefold symmorphic rotation symmetries (i.e., $p = 0$ in $C_{3,p}$). Consequently, the eigenvalues of these symmorphic rotation symmetries are momentum independent and hence there are no symmetry-enforced Weyl points for *R*-trigonal space groups.

B. Compatibility relations between irreps

Next, we explain how the existence of symmetry-enforced Weyl points can be derived from the compatibility relations of irreducible representations (irreps) at different high-symmetry points/lines of the BZ [49–51]. Here, we give a brief outline of this derivation for SG No. 144 ($P3_1$). Additional details can be found in Ref. [39].

Bloch bands $|\psi_m(\vec{k})\rangle$ restricted to a high-symmetry line (or point) can be labeled by the irreducible representations (irreps) of the symmetry operators that leave this line (or point) invariant. An irrep of a given symmetry group can be viewed as a set of matrices which form a group that is homomorphic to the symmetry group, with the property that there does not exist a unitary transformation that brings all these matrices into block diagonal form. While these sets of matrices are not unique, their trace (i.e., their character) is unchanged under any unitary transformation. Therefore, for a given high-symmetry line (or point) in the BZ one can define a character table, which lists the irreps and their characters for all the symmetry operations that leave this line (or point) invariant.

Now, as we move from a high-symmetry point to a high-symmetry line in the BZ, the symmetry is lowered, and hence an irrep A_σ of the high-symmetry point is, in general, no longer irreducible for the high-symmetry line. That is, the irrep A_σ of the high-symmetry point decomposes, in general, into smaller irreps $B_{i,\sigma}$ of the high-symmetry line. However, under such a decomposition the character χ of each relevant symmetry must be preserved, i.e.,

$$\chi(A_\sigma) = \sum_{i=1}^{n} \chi(B_{i,\sigma}). \tag{2.3}$$

The above equation defines the *compatibility relations* between the irreps A_σ at a high-symmetry point and the irreps $B_{i,\sigma}$ at a high-symmetry line [52,53].

TABLE III. Double-valued irreps for SG No. 144 ($P3_1$) without time-reversal symmetry at the points Γ and A and at the line Δ. For the labeling of the irreps we use the same convention as in Ref. [51].

Irreps/Symmetry Element	C_3
$\bar{\Gamma}_4$	-1
$\bar{\Gamma}_5$	$e^{-i\pi/3}$
$\bar{\Gamma}_6$	$e^{i\pi/3}$
$\bar{\Delta}_4$	$e^{ik_z/3}$
$\bar{\Delta}_5$	$e^{i(k_z-\pi)/3}$
$\bar{\Delta}_6$	$e^{i(k_z+\pi)/3}$
$\bar{A}_4$	$e^{-i2\pi/3}$
$\bar{A}_5$	$+1$
$\bar{A}_6$	$e^{i2\pi/3}$

We shall now use these compatibility relations to study how the irreps decompose in SG No. 144 ($P3_1$) for the path Γ-Δ-A, which is left invariant under the screw rotation $C_{3,1}$. Since we are interested in electronic band structures with spin-orbit coupling, we need to consider the *double-valued* irreps of SG No. 144 ($P3_1$) (see Table III), as the identity operator is not equivalent to a rotation by 2π but rather by 4π on the Bloch sphere. At the time-reversal invariant momenta (TRIMs), Bloch bands form Kramers pairs due to time-reversal symmetry. This means that at the TRIMs pairs of complex conjugate irreps combine together to form a time-reversal symmetric irrep [52,53]. For the $1d$ irreps of Table III we can construct these time-reversal symmetric irreps by inspection. At the Γ point we find that the time-reversal symmetric irreps are given by the direct product of $\bar{\Gamma}_5$ with $\bar{\Gamma}_6$ and $\bar{\Gamma}_4$ with itself. Similarly, at the A point the time-reversal symmetric irreps are given by the direct product of $\bar{A}_4$ with $\bar{A}_6$ and $\bar{A}_5$ with itself; see Fig. 1(c). As we move from the TRIMs Γ and A to a point on the high-symmetry line Δ, the two-dimensional time-reversal symmetric irreps decompose into one-dimensional irreps, according to Eq. (2.3); see left part of Fig. 1(c). Connecting the respective irreps that split away from the points Γ and A we find that the bands connect in a nontrivial way, with a minimum number of two Weyl point crossings, as shown in the right part of Fig. 1(c). This is in exact agreement with the symmetry analysis presented above. A similar analysis can be done for the remaining five space groups of Table I and we find perfect agreement therein.

C. Weyl point multiplicities

So far we have only discussed the appearance of Weyl points on the Γ-Δ-A line. However, it follows from symmetry arguments together with the fermion-doubling theorem [54] that these cannot be the only Weyl points in the BZ. This is because (i) there has to be another Weyl point away from the Γ-Δ-A line with opposite chirality, since the chiralities of all Weyl points formed by one pair of bands must cancel out to zero [54], and (ii) time-reversal and SG symmetries lead to additional copies of the Weyl points that are located away from the Γ-Δ-A line. Using these arguments, we now determine for each SG the minimum number of Weyl points that is compatible with the symmetries and the fermion-doubling theorem. To do so, we first note that we can divide the BZ into two parts, an upper part with $k_z \in [0, \pi]$ and a lower part with $k_z \in [-\pi, 0]$, which are related by time-reversal symmetry. Hence, it is sufficient to analyze the Weyl point configuration in the upper part; the configuration in the lower part can be obtained by applying time-reversal symmetry (see Fig. 2). For concreteness, we assume in the following that the Weyl points at the Γ-Δ-A line have positive chirality $+1$.

a. SG Nos. 144, 145, 151, and 153. Band structures in SG Nos. 144 and 145 possess only two symmetries: the threefold screw rotation along the k_z axis $C_{3,p}$ and time-reversal symmetry. In order to cancel the $+1$ chirality of the Weyl point at the Γ-Δ-A line, we need to place a negative chirality Weyl point somewhere else in the BZ. If we put it at an arbitrary position, the screw rotation $C_{3,p}$ would generate two more copies with the same chirality, leading to an overcompensation. Instead, in order to construct a Weyl point configuration with minimal multiplicity, we need to put the negative chirality Weyl point at one of the other two $C_{3,p}$-invariant lines, i.e., either on K-P-H or on K'-P'-H'. With this, the chiralities cancel out and we obtain a minimal Weyl point multiplicity of 4; see Fig. 2(a). We note that the existence of Weyl points on K-P-H and K'-P'-H' can also be inferred from the k_z dependence of the $C_{3,p}$ eigenvalues. For a discussion on this see Appendix C.

SG Nos. 151 and 153 possess an additional twofold screw rotation along the k_y axis, which however does not affect the above argument. Hence, also in these SGs the minimal Weyl point multiplicity is 4.

b. SG Nos. 152 and 154. SG Nos. 152 and 154 contain, besides the threefold screw rotation $C_{3,p}$, a twofold rotation C_2 along the (110) axis, which maps $(k_x, k_y, k_z) \to (k_x, -k_y, -k_z)$. This C_2 rotation puts extra constraints on the multiplicity of the Weyl points. To find these constraints we combine the C_2 rotation with time-reversal symmetry, yielding the mirror symmetry $(k_x, k_y, k_z) \to (-k_x, k_y, k_z)$ [dashed lines in Fig. 2(b)]. If we now put a negative chirality Weyl point on the K-P-H line, the mirror symmetry would generate another negative chirality Weyl point at the K'-P'-H' line, leading to an overcancellation. Instead we place positive chirality Weyl points both at K-P-H and K'-P'-H', which we then compensate by negative chirality Weyl points on the three mirror planes, as shown in Fig. 2(b). This configuration of 12 Weyl points has minimal multiplicity, satisfies all the symmetries, and has zero total chirality.

III. NONSYMMORPHIC NODAL LINES

Using the techniques discussed in the previous section we will now prove that glide-reflection symmetries lead to symmetry-enforced nodal lines in materials with trigonal space groups. As before, this derivation is based on (i) the momentum dependence of the symmetry eigenvalues and (ii) the compatibility relations between irreps.

A. Symmetry eigenvalues

We consider glide-mirror symmetries M with a fractional shift of one-half of the lattice constant along the z axis. Applying these symmetries twice we obtain $M^2 = -\hat{z}$, where the minus sign is due to the 2π rotation of the electron spin.

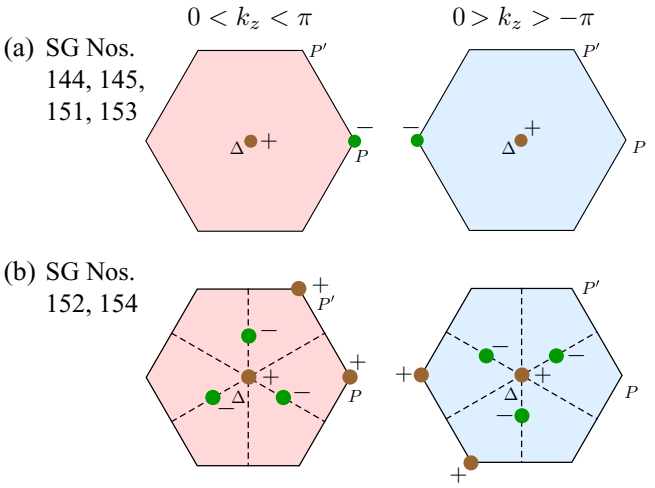

FIG. 2. Weyl point configuration with minimal multiplicity for the six trigonal SGs with symmetry-enforced Weyl points (see Table I). The red and blue hexagons represent the top view of the upper and lower parts of the hexagonal BZ, which are related by time-reversal symmetry. The brown and green dots indicate the positions of the Weyl points with positive and negative chirality, respectively. (a) In SG Nos. 144, 145, 151, and 153 the minimal Weyl point multiplicity is 4. Weyl points with the same chirality are related by time-reversal symmetry. (b) In SG Nos. 152 and 154 the minimal Weyl point multiplicity is 12. Weyl points with the same chirality are related by time-reversal symmetry and the mirror symmetries indicated by the dashed lines.

From this it follows that the eigenvalues of the Bloch wave functions in the mirror planes are given by

$$M|\psi_\pm(\vec{k})\rangle = \pm ie^{-ik_z/2}|\psi_\pm(\vec{k})\rangle. \tag{3.1}$$

The mirror planes contain either two or four TRIMs at which the Bloch bands are Kramers degenerate (blue and red dots in Fig. 3). It follows from Eq. (3.1) that the M eigenvalues of the Bloch bands at the TRIMs A, L, and Z are ± 1, while at the TRIMs Γ, M, and F they are $\pm i$. Due to the antiunitary time-reversal symmetry, at Γ, M, and F the Kramers pairs are formed between bands with opposite M eigenvalues (blue dots), while at A, L, and Z they are formed between bands with the same eigenvalues (red dots). Hence, as we move from a blue TRIM to a red TRIM the Kramers pairs must switch partners. In the absence of additional symmetries this leads to a nontrivial band connectivity with a symmetry-enforced band crossing [see Fig. 3(a)]. Since this is true for any path connecting a blue TRIM to a red TRIM, the Weyl band crossings occur along a one-dimensional line separating the blue TRIMs from the red TRIMs [see Figs. 3(b)–3(d)]. We note that the presence of additional symmetries, in particular inversion, leads to additional degeneracies, thereby invalidating the above argument. Thus, symmetry-enforced nodal lines only occur in SGs with a mirror-glide symmetry but no inversion symmetry. Among the trigonal SGs there are only three SGs satisfying these criteria, namely Nos. 158, 159, and 161.

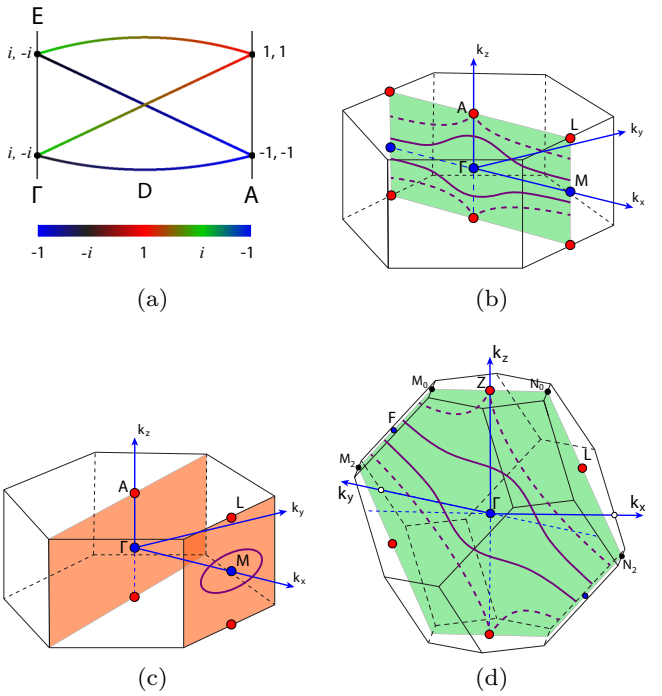

FIG. 3. (a) Band connectivity diagram for a path within the k_xk_z plane of the hexagonal BZ of SG No. 158 connecting Γ to A [see panel (b)]. The color indicates the glide-mirror eigenvalues (3.1) of the Bloch bands. (b)–(d) Weyl nodal lines (purple solid and dashed curves) protected by glide-mirror symmetries for (b) SG No. 158, (c) SG No. 159, and (d) SG No. 161 are shown in the respective bulk BZs. The TRIMs are indicated by the blue and red dots and the mirror planes are shown in green and orange. For SG Nos. 158 and 161 there are two nodal lines separating the blue from the red TRIMs. Depending on the dimensionality of the irreps at the A point (Z point) these nodal lines either touch (dashed curves) or do not touch (solid curves) the A point (Z point). In SG No. 159 there is a nodal line in the $k_x = \pi$ plane enclosing a single TRIM. Note that there are different possibilities for the shape and connectivity of the nodal lines; here we only show the simplest one.

SG No. 158 ($P3c1$) has hexagonal lattice system (P-trigonal) and contains the glide-mirror symmetry

$$M_{010} : (x, y, z) \to \left(x, x - y, z + \frac{1}{2}\right) \otimes \left(-\frac{i\sqrt{3}}{2}\sigma_x - \frac{i}{2}\sigma_y\right), \tag{3.2}$$

which leaves the k_xk_z plane invariant. Following the above arguments we find that this glide-mirror symmetry leads to two nodal loops in the k_xk_z plane, which separate the red TRIMs from the blue TRIMs, as shown in Fig. 3(b). If the irrep at the A point has dimension 4 (instead of 2), these nodal lines touch the A point [dashed curve in Fig. 3(b)]. We note that these nodal loops must be symmetric under time-reversal symmetry and the point-group operations of SG No. 158, but are otherwise free to move within the mirror plane.

SG No. 159 ($P31c$) also has a hexagonal lattice system (P-trigonal) and contains the glide-mirror symmetry

$$M_{210} : (x, y, z) \to \left(-x, -x + y, z + \frac{1}{2}\right) \otimes \left(\frac{i}{2}\sigma_x + \frac{i\sqrt{3}}{2}\sigma_y\right), \tag{3.3}$$

TABLE IV. Double-valued irreps of SG No. 158 ($P3c1$) without time-reversal symmetry at the TRIMs Γ, A, M, and L and the plane D (i.e., the k_xk_z plane); see Fig. 3(b). We use the same convention as in Ref. [51] for labeling the irreps.

Irreps/Symmetry Element	M_{010}
$\bar{\Gamma}_4$	$-i$
$\bar{\Gamma}_5$	$+i$
$\bar{\Gamma}_6$	$\begin{pmatrix} 0 & e^{-i\pi/3} \\ e^{-i2\pi/3} & 0 \end{pmatrix}$
$\bar{A}_4$	$+1$
$\bar{A}_5$	-1
$\bar{A}_6$	$\begin{pmatrix} 0 & e^{i\pi/6} \\ e^{-i\pi/6} & 0 \end{pmatrix}$
$\bar{M}_3$	$-i$
$\bar{M}_4$	$+i$
$\bar{D}_3$	$-ie^{ik_z/2}$
$\bar{D}_4$	$+ie^{ik_z/2}$
$\bar{L}_3$	$+1$
$\bar{L}_4$	-1

which leaves both the $k_x = 0$ and the $k_x = \pi$ planes invariant; see Fig. 3(c). Both mirror planes have two TRIMs, between which the Kramers pairs change partners. Hence, according to the above arguments, there should be nodal lines in both mirror planes, which encircle either the Γ/M or A/L points. However, at the A point there exist four-dimensional irreps, leading to a fourfold band degeneracy. For this reason, symmetry-enforced nodal lines generically occur only in the $k_x = \pi$ plane, but not in the $k_x = 0$ plane [55].

SG No. 161 ($R3c$) has a rhombohedral lattice system (R-trigonal) and contains the glide-mirror symmetry

$$M_{110} : (x, y, z) \to \left(-y, -x, z + \frac{1}{2}\right) \otimes \left(-\frac{i\sqrt{3}}{2}\sigma_x - \frac{i}{2}\sigma_y\right), \tag{3.4}$$

which leaves the plane $k_x = -k_y$ invariant; see Fig. 3(d). As in SG No. 158, this glide-mirror symmetry gives rise to two nodal lines separating the two red TRIMs from the two blue TRIMs. If the bands transform at the Z point under an irrep with dimension 4 (instead of 2), then the nodal lines touch the Z point [dashed curve in Fig. 3(d)].

B. Compatibility relations between irreps

The existence of symmetry-enforced nodal lines can also be derived from the compatibility relations between irreps. Here, we present this derivation for SG No. 158 ($P3c1$). The derivation for SG Nos. 159 and 161 proceeds in a very similar way.

For SG No. 158 the relevant high-symmetry plane is the plane D (i.e., the k_xk_z plane), which is left invariant under the glide-mirror symmetry M_{010}, Eq. (3.2). This mirror plane contains the four TRIMs Γ, A, L, and M. To determine the connectivity of the bands we first need to derive the irreps at these four TRIMs and at the D plane. The double-valued irreps without time-reversal symmetry are listed in Table IV. We find that these irreps are all complex with the exception of $\bar{\Gamma}_6$, which is pseudoreal. Pseudoreal irreps are time-reversal invariant by themselves, while complex irreps need to be paired up to construct time-reversal invariant irreps [52,53] (cf. Fig. 4). Note that at the A point there are both two-dimensional and four-dimensional time-reversal invariant irreps. The decomposition of these time-reversal invariant irreps, as we move from a TRIM to a nearby point in the mirror plane D, can be inferred from Eq. (2.3), or alternatively from the program DCOMPREL on the Bilbao Crystallographic Server [51]. The resulting compatibility relations are depicted in Figs. 4(a), 4(c), and 4(e). Using these compatibility relations, we can now construct the band connectivity diagrams for a path within the D plane that connects two TRIMs; see Figs. 4(b), 4(d), and 4(f). We observe that for any path connecting Γ/M to L, there must be at least one band crossing. The same is true for paths connecting Γ to A or M to A, albeit here the band crossings can be pinned at the A point, if the corresponding irrep is four-dimensional. Hence, the D plane must contain at least two Weyl nodal lines enclosing the Γ and M points, as shown in Fig. 3(b).

IV. FILLING CONSTRAINTS

According to band theory, a noninteracting band insulator can only exist if the electron filling ν is an even integer, i.e., $\nu \in 2\mathbb{N}$. Vice versa, materials with $\nu \notin 2\mathbb{N}$ must necessarily be (semi)metals. In materials with nonsymmorphic symmetries, however, these filling constraints are more rigid. This is because nonsymmorphic symmetries enforce band crossings that lead to groups of more than two connected bands. Thus, using the analysis from Secs. II and III we can derive the more rigid filling constraints. For example, for SG No. 144 ($P3_1$) we observe that along the Γ-Δ-A line six bands form a connected group. Thus, in an insulator with SG No. 144 this group of six bands must be fully filled, i.e., the electron filling ν must be an element of $6\mathbb{N}$. Using these arguments we have derived the filling constraints for all the nonsymmorphic trigonal space groups; see fourth column of Table I. These results are in full agreement with the analysis of Ref. [45].

V. EXAMPLE MATERIALS

Having identified the SGs whose nonsymmorphic symmetries enforce Weyl points and Weyl nodal lines, we can now perform a database search for materials in these SGs. We look for suitable compounds in the ICSD database [56], the AFLOW database [57], and the Materials Project database [58,59], which yields four materials with accordion Weyl points and one material with Weyl nodal lines. Unfortunately, none of these four materials are really ideal, since their band crossings are far away in energy from the Fermi level. Hence, we are not proposing these materials as practical new semimetals, but use them only to illustrate the predicted band crossings in an existing compound.

For each of these example materials we perform electronic band structure calculations with the Vienna *ab initio* simulation package (VASP) [60,61], using the projector augmented wave (PAW) method [62,63] and the PBE [64] and mBJ [65,66] exchange-correlation functionals. As input for the *ab initio* calculations we use the experimental crystal structures of Refs. [67–71]. In the following we discuss the band structures along those high-symmetry lines/planes where the predicted band crossings occur. The full band structures along

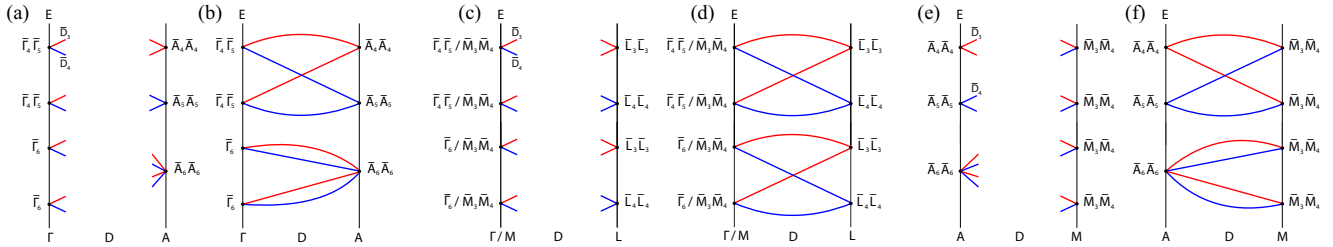

FIG. 4. (a), (c), (e) Kramers pairings and compatibility relations for SG No. 158 ($P3c1$) between the irreps at the TRIMs and at a point in the mirror plane D (i.e., a point in the $k_x k_z$ plane). (b), (d), (f) Band connectivity diagrams for SG No. 158 for paths within the D plane connecting two TRIMs. Due to these nontrivial band connectivities the D plane must contain at least two Weyl nodal lines; see Fig. 3(b).

all high-symmetry directions of the BZ are presented in Appendix A. For two examples we also compute surface states using tight-binding models constructed from Wannier functions [72].

A. Materials with Weyl nodal points

Here, we present four materials which exhibit Weyl nodal points with accordion-like dispersions.

a. Cu_2SrSnS_4 *and* Cu_2SrGeS_4. The chalcogenide Cu_2SrSnS_4, which crystallizes in SG No. 144 ($P3_1$) [67,73], is an example of a material with Weyl points along the Γ-Δ-A line, as discussed in Sec. II. The electronic band structure computed with the mBJ functional, see Figs. 5 and 10(a), shows a band gap of about 1.1 eV, which is somewhat smaller than the experimentally reported value of 1.78 eV [73]. We observe in Fig. 5 that there are groups of $6n$ connected bands between Γ and A, which form a large number of Weyl points. This is in full agreement with the band connectivity diagrams of Figs. 1(b) and 1(c). The Weyl points of Cu_2SrSnS_4 are symmetry protected by the screw rotation $C_{3,1}$, Eq. (2.1). Their topological stability is ensured by quantized Chern numbers. Due to the bulk-boundary correspondence, these Chern numbers lead to arc surface states. Unfortunately, due to the large band gap of ∼1.8 eV, it will be very challenging to probe the bulk Weyl points or arc surface states of Cu_2SrSnS_4 using photoemission, tunneling spectroscopy, or transport experiments. Perhaps, one could try to grow Cu_2SrSnS_4 as a thin film on a conducting substrate, which might allow one to probe the Weyl points using photoemission.

Cu_2SrGeS_4 is very similar to Cu_2SrSnS_4. It crystallizes in SG No. 145 ($P3_2$) [68] and its band structure shows a large number of Weyl points along the Γ-Δ-A line; see Fig. 10(b).

b. Ag_2HPO_4. Silver hydrogen phosphate with the chemical formula Ag_2HPO_4 is a salt that crystallizes in SG No. 151 [69]. According to our analysis of Sec. II, band structures with this SG symmetry exhibit Weyl points along the Γ-Δ-A line. Figures 6 and 10(c) display the first-principles band structure of Ag_2HPO_4, computed with the mBJ functional. The band structure shows a band gap of about 2.8 eV. Along the Γ-Δ-A direction we observe a group of 24 ($= 6 \times 4$) connected bands, with many crossings, similar to the band connectivity diagrams of Fig. 1. These band crossings are Weyl points, whose topology is characterized by a nonzero Chern number. The nontrivial topology of these Weyl points gives rise to arc states at the surface, which connect Weyl points with opposite chirality. In Fig. 7 we demonstrate this for the Weyl point marked by the gray circle in Fig. 6. At the (-110) surface we observe an arc state that emanates out from the projected Weyl point.

While the *ab initio* band structure of Ag_2HPO_4 nicely illustrates the predicted accordion states, this material is rather unsuitable for experimental investigations. Its large band gap

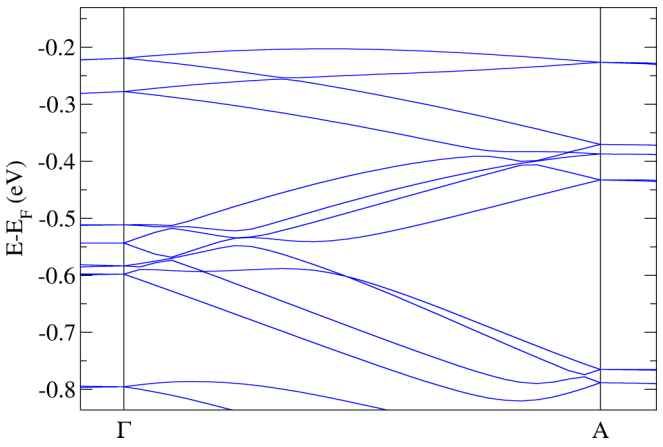

FIG. 5. Electronic band structure of Cu_2SrSnS_4 in SG No. 144 ($P3_1$) computed with the mBJ functional [65,66]. The band crossings along the Γ-Δ-A line are symmetry-enforced by the screw rotation $C_{3,1}$; see Sec. II.

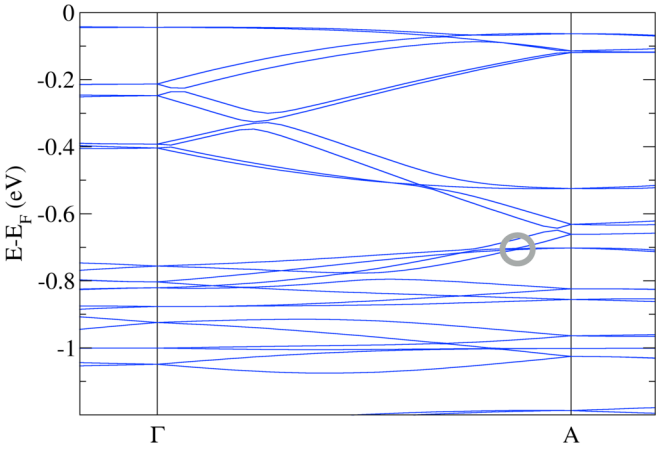

FIG. 6. First-principles band structure of silver hydrogen phosphate Ag_2HPO_4 in SG No. 151 ($P3_112$) computed with the mBJ functional. The band crossings along the Γ-Δ-A line are Weyl points that are symmetry-enforced by the screw rotation $C_{3,1}$ (see Sec. II).

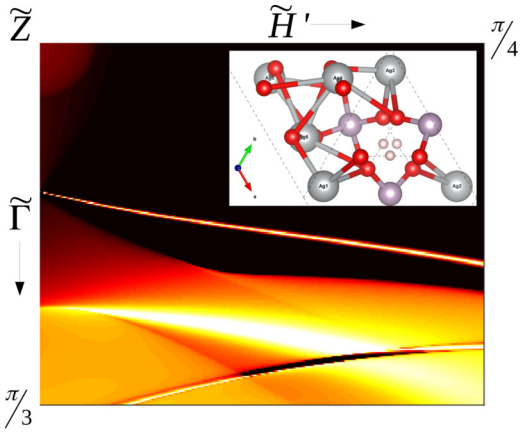

FIG. 7. Momentum-dependent surface density of states for the (-110) surface of Ag_2HPO_4 at the energy $E - E_F = -0.704$ eV. The crystal is terminated such that the silver atoms Ag3, Ag4, and Ag5 are at the top layer (see crystal structure in inset). Yellow and black correspond to high and low densities, respectively. The location of the projected Weyl point is marked by a gray circle; cf. Fig. 6. For a plot of the (-110) surface BZ, see Fig. 1(a).

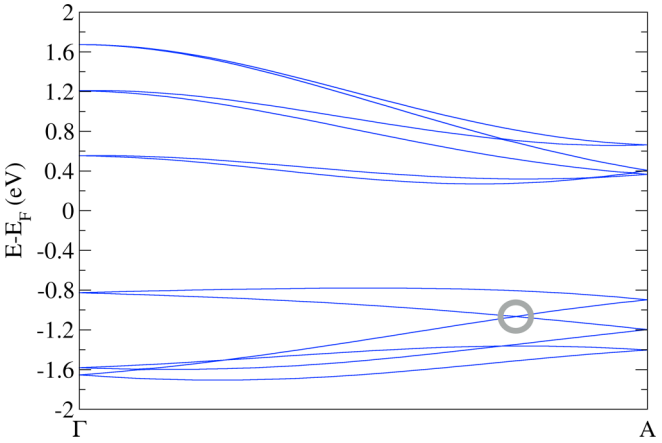

FIG. 8. Electronic band structure of trigonal tellurium in SG No. 152 ($P3_121$), computed with the PBE functional. The band crossings with accordion dispersions along the Γ-Δ-A line are symmetry-enforced by the screw rotation $C_{3,1}$ (see Sec. II).

and the fact that it cannot be doped easily make it experimentally impossible to probe the bulk Weyl points and arc surface states.

c. Te. At ambient conditions, elemental tellurium (Te) has a trigonal crystal structure with SG No. 152 ($P3_121$) [70,74]. In this structure the Te atoms form helical chains along the z direction, which are arranged in a hexagonal array [75]. Recent first-principles calculations have shown that the valence and conduction bands of Te at the H point exhibit several Weyl points [36,76,77]. Moreover, it was found that hydrostatic or uniaxial strain leads to a band inversion at the H point, thereby transforming Te into a strong topological insulator [78].

It follows from our analysis of Sec. II, that Te exhibits Weyl points not only at the H point, but also along the Γ-Δ-A line, which is left invariant by the screw rotation $C_{3,1}$. This is clearly visible in the *ab initio* band structure calculations of Figs. 8 and 10(d), which show Weyl points with accordion-like dispersions between Γ and A. As before, we observe that the band connectivity fully agrees with the theoretical prediction of Fig. 1. By the bulk-boundary correspondence, the Weyl points at the H point and on the Γ-Δ-A line lead to numerous arc surface states; see Appendix B. These arc surface states should be readily observable in photoemission and scanning tunneling experiments.

In closing, we note that trigonal selenium (Se), which also crystalizes in SG No. 152 ($P3_121$) [79], has a very similar band structure to tellurium, albeit the spin-orbit coupling is considerably smaller Fig. 10(e). Therefore, the bands forming Weyl points along the Γ-Δ-A line of Se are only separated by less than ∼50 meV. This makes the experimental detection of the accordion Weyl points in Se more challenging than in Te.

B. Weyl nodal lines in $Te_{16}Si_{38}$

The tellurium-silicon clathrate $Te_{16}Si_{38}$ crystallizes in two different forms. While the low-temperature form is cubic, the high-temperature form is rhombohedral with trigonal SG No. 161 ($R3c$) [71,80]. According to our analysis of Sec. III, materials in this SG exhibit Weyl nodal lines that are protected by the glide-mirror symmetry M_{110}. In Fig. 9 we present the first-principles band structure (with PBE functional) of rhombohedral $Te_{16}Si_{38}$ along high-symmetry paths of the $k_x = -k_y$ plane, which is left invariant by M_{110} [see also Fig. 10(f)]. We observe that along any path that connects a blue TRIM to a red TRIM in the BZ of Fig. 3(d), $4n$ bands form a connected group with many Weyl crossings. These Weyl crossings are part of Weyl nodal lines that separate the blue from the red TRIMs in the $k_x = -k_y$ plane. The stability of these Weyl nodal lines is guaranteed by a π-Berry phase, which by the bulk-boundary correspondence gives rise to drumhead surface states [81]. In addition, the bands of rhombohedral $Te_{16}Si_{38}$ carry a nonzero Berry curvature which becomes especially large close to the Weyl nodal lines.

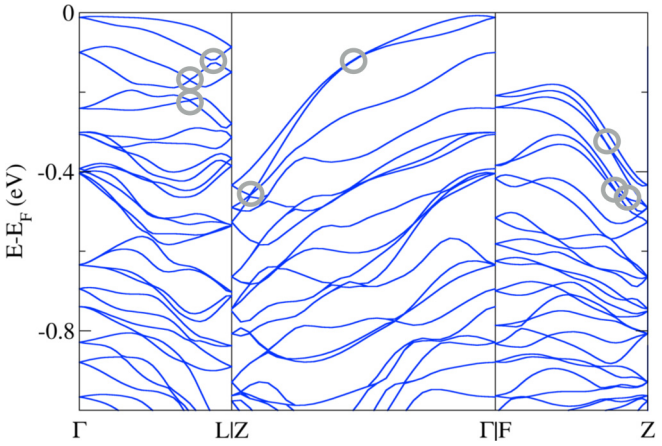

FIG. 9. DFT-PBE band structure of rhombohedral $Te_{16}Si_{38}$ along high-symmetry paths of the $k_x = -k_y$ plane of the rhombohedral BZ [see Fig. 3(d)]. The band crossings (marked by gray circles for the top few bands) are part of Weyl nodal lines, which are protected by the glide-mirror symmetry M_{110}.

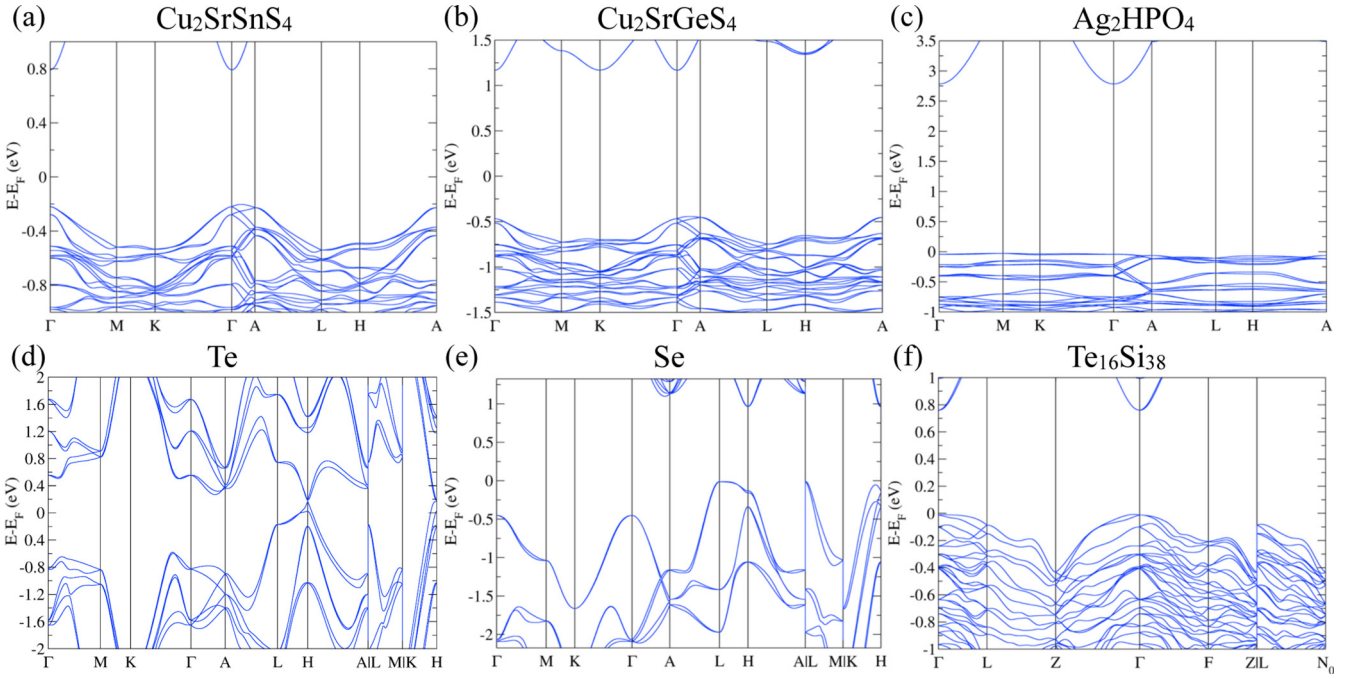

FIG. 10. (a), (b), (c) DFT band structures computed with the mBJ functional for Cu_2SrSnS_4, Cu_2SrGeS_4, and Ag_2HPO_4. Along the Γ-Δ-*A* line, these materials exhibit Weyl points with accordion dispersions. For a zoom-in of the band structure near the Weyl points see Sec. V A in the main text. (d), (e) DFT-PBE band structure of trigonal tellurium and selenium. Along the Γ-Δ-*A* direction there are groups of six connected bands, which cross at several Weyl points. (f) DFT-PBE band structure for $Te_{16}Si_{38}$, which exhibits Weyl nodal lines within the $k_x = -k_y$ plane. For a zoom-in of the band structure around the Weyl nodal lines, see Fig. 9 in the main text.

VI. CONCLUSIONS

In summary, we have performed a systematic analysis of nonsymmorphic band crossings in nonmagnetic trigonal materials with strong spin-orbit coupling. We have found that among the 25 trigonal space groups, six support Weyl points, while three support Weyl nodal lines (see Table I). The electronic bands at these Weyl points and Weyl lines are required to cross due to nonsymmorphic mirror or rotation symmetries alone, regardless of the chemical composition and other material details. Hence, these Weyl crossings occur in all bands of any material crystallizing in the space groups listed in Table I. Using this insight, we have performed a database search and identified several existing materials that possess the predicted topological band crossings; see the last column in Table I. The nontrivial topology of the band crossings in these materials leads to a number of interesting and experimentally observable phenomena, e.g., arc and drumhead surface states, anomalous magnetotransport properties, and anomalous Hall effects. Particularly interesting are the nonsymmorphic band crossings and surface states of tellurium (Figs. 8 and 11). We hope that our findings will encourage experimentalists to study the topological properties of these compounds.

ACKNOWLEDGMENTS

The authors thank C. Ast, K. von Klitzing, A. Topp, M. G. Vergniory, and A. Yaresko for useful discussions. B.K. thanks the Max Planck Institute for Solid State Research in Stuttgart for financial support. This research was supported in part by the National Science Foundation under Grant No. NSF PHY-1748958. C.-K.C. is supported by the Strategic Priority Research Program of the Chinese Academy of Sciences (Grant No. XDB28000000). Work at Princeton was supported by NSF through the Princeton Center for Complex Materials, a Materials Research Science and Engineering Center, Grant No. DMR-1420541.

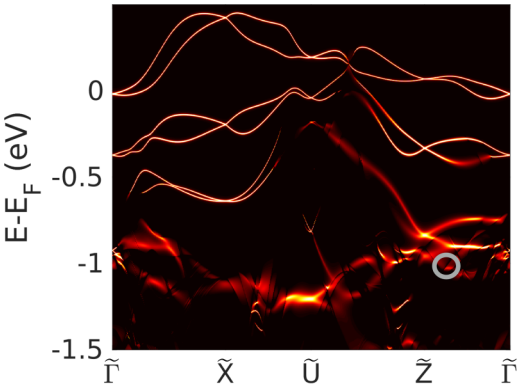

FIG. 11. Energy dispersion of the surface states of trigonal tellurium for the (-110) surface along high-symmetry momentum directions; cf. Fig. 1(a). The color grading indicates the surface density of states, with yellow and black corresponding to high and low densities, respectively. The gray circle denotes the projected position of the Weyl point at the energy $E - E_F = -1.072$ eV; see Fig. 8.

APPENDIX A: ADDITIONAL BAND STRUCTURE CALCULATIONS

In this Appendix, we present additional band structure calculations for the example materials studied in Sec. V of the main text. In Figs. 10(a), 10(b), and 10(c), we present the full band structures of the materials Cu_2SrSnS_4, Cu_2SrGeS_4, and Ag_2HPO_4, respectively, which exhibit Weyl points along Γ-Δ-A. These Weyl points are symmetry enforced by the threefold $C_{3,p}$ screw rotations. In the chalcogenides Cu_2SrSnS_4 and Cu_2SrGeS_4 the band gap is about 1.5 eV, while in the salt Ag_2HPO_4 it is about 2.8 eV. This makes it challenging to observe the Weyl points in photoemission or electron tunneling experiments. However, it might be perhaps possible to grow thin films of Cu_2SrSnS_4 and Cu_2SrGeS_4 on a conducting substrate to introduce charge carriers.

Figures 10(d) and 10(e) display the full band structures of trigonal tellurium and selenium. Along the Γ-Δ-A line there are groups of six connected bands with accordion dispersions. Since tellurium is metallic, it should be possible to observe its accordion dispersion and Weyl points using angle-resolved photoemission experiments. Tellurium has many Weyl points also away from the Γ-Δ-A line, for example, at the H point [76,77]. These give rise to numerous arc surface states; see Appendix B.

Figure 10(f) shows the full band structure of the tellurium-silicon clathrate $Te_{16}Si_{38}$, which exhibits Weyl nodal lines in the $k_x = -k_y$ plane. We observe that along the paths Γ-L, Γ-Z, and F-Z, the bands form groups of $4n$ connected bands with Weyl crossings. These Weyl crossings are part of nodal lines that separate Γ and F from Z and L in the $k_x = -k_y$ plane of the rhombohedral BZ; see Fig. 4(d).

APPENDIX B: SURFACE STATES OF TELLURIUM

Trigonal tellurium has many Weyl points and associated arc surface states. In Fig. 11 we present the surface state dispersion for the (-110) surface of Te [82]. The labels of the high-symmetry points in the (-110) surface BZ are given in Fig. 1(a). We observe that there are several surface states emanating from the Weyl points near the H point. Remarkably, these surface states cross the entire surface BZ and lie within the bulk band gap, in between the valence and conduction bands. Since their energy is close to the Fermi level, they could play an important role for the (re)interpretation of the unusual surface transport and photoemission measurements reported in Refs. [83–85].

There are also arc surface states that are associated with the accordion bands discussed in Sec. V A (paragraph *c*) and Fig. 8. For example, for the topmost Weyl point in the valence bands at the energy $E - E_F = -1.072$ (gray circle in Fig. 8), we observe an arc state that disperses toward the $\tilde{\Gamma}$ point.

APPENDIX C: SYMMETRY-ENFORCED BAND CROSSING ON THE *K*-*P*-*H* AND *K*′-*P*′-*H*′ LINES

In Sec. II C, we have inferred the existence of Weyl points on the K-P-H and K'-P'-H' lines by use of the fermion doubling theorem. Here, we show that the existence of Weyl points on K-P-H and K'-P'-H' lines can also be deduced from the k_z dependence of the $C_{3,p}$ eigenvalues. For concreteness, we focus here on SG Nos. 144, 145, 151, and 153, which possess a threefold screw rotation $C_{3,p}$ along the k_z axis. The eigenvalues of the $C_{3,p}$ screw rotation are given by

$$C_{3,p=1}|\psi_m(\mathbf{k})\rangle = e^{-ik_z/3+i\pi(2m+1)/3}|\psi_m(\mathbf{k})\rangle, \tag{C1}$$

where the eigenvalue label m is an element of $m \in \{0, 1, 2\}$. It follows that as k_z runs from $-\pi$ to $+\pi$, the eigenstates $|\psi_m(\mathbf{k})\rangle$ are transformed into each other as follows:

$$\begin{aligned} |\psi_0(\mathbf{k})\rangle &\to |\psi_2(\mathbf{k})\rangle, \\ |\psi_1(\mathbf{k})\rangle &\to |\psi_0(\mathbf{k})\rangle, \\ |\psi_2(\mathbf{k})\rangle &\to |\psi_1(\mathbf{k})\rangle. \end{aligned} \tag{C2}$$

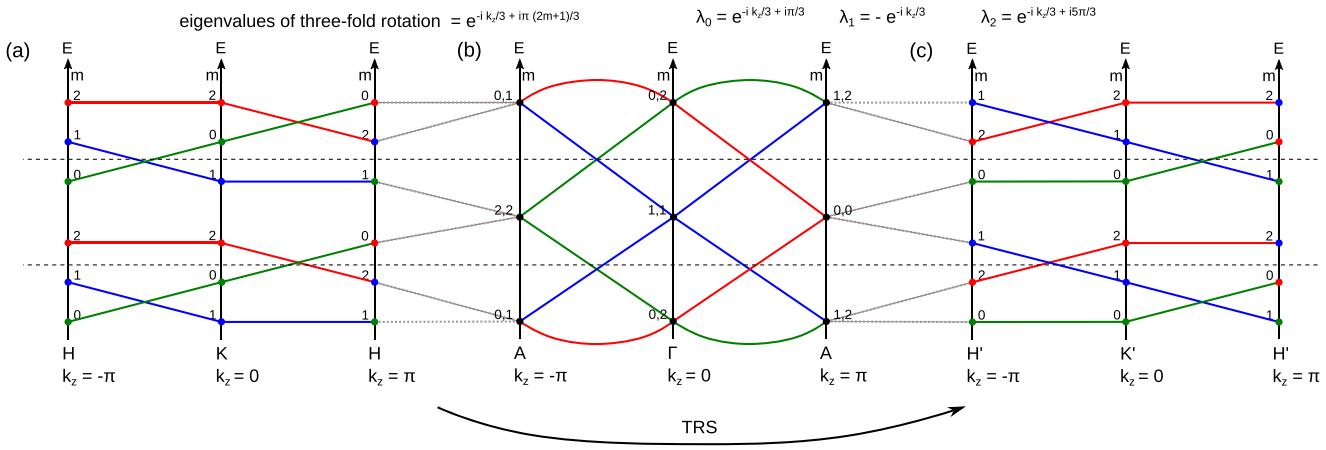

FIG. 12. Band connectivity along the H-K-H, A-Γ-A, and H'-K'-H' lines, which are left invariant by the $C_{3,p}$ screw-rotation symmetry. The three eigenstates $|\psi_0(\mathbf{k})\rangle$ (green), $|\psi_1(\mathbf{k})\rangle$ (blue), and $|\psi_2(\mathbf{k})\rangle$ (red) of the $C_{3,p}$ screw rotation switch between $k_z = -\pi$ and $k_z = +\pi$ of the H-K-H and H'-K'-H' lines, according to Eq. (C2). Therefore the bands must cross as shown in panels (a) and (c). Along the A-Γ-A line the band connectivity is of the accordion type, as discussed in Sec. II A. Note that this figure shows only one possible arrangement of the band crossings. Other arrangements consistent with Eq. (C2) are possible, but they all have a minimum of four band crossings on H-K-H, H'-K'-H', and A-Γ-A (not counting the Kramers degeneracies at the TRIMs).

Hence, the eigenstates switch as one moves once through the BZ along the H-K-H or H'-K'-H' lines. Therefore, the three eigenstates $|\psi_0(\mathbf{k})\rangle$, $|\psi_1(\mathbf{k})\rangle$, and $|\psi_2(\mathbf{k})\rangle$ must cross each other at least twice on the H-K-H and H'-K'-H' lines, as shown in Figs. 12(a) and 12(b). The chiralities of the Weyl points on the dashed lines in Fig. 12 cancel each other, such that the fermion-doubling theorem is satisfied. That is, if the chirality of the Weyl points on A-Γ-A is, say, positive, then the chirality of the Weyl points on H-K-H and H'-K'-H' must be negative.

[1] Throughout this paper we use the term "band crossing" to denote any point or line in the Brillouin zone where two bands are degenerate. This includes also Weyl points (also known as "Weyl nodes").

[2] C.-K. Chiu, J. C. Y. Teo, A. P. Schnyder, and S. Ryu, Rev. Mod. Phys. **88**, 035005 (2016).

[3] G. E. Volovik, *Topology of Quantum Vacuum*, Lecture Notes in Physics, Vol. 870 (Springer, Berlin, 2013), pp. 343–383.

[4] N. P. Armitage, E. J. Mele, and A. Vishwanath, Rev. Mod. Phys. **90**, 015001 (2018).

[5] A. Burkov, Annu. Rev. Condens. Matter Phys. **9**, 359 (2018).

[6] S.-Y. Yang, H. Yang, E. Derunova, S. S. P. Parkin, B. Yan, and M. N. Ali, Adv. Phys.: X **3**, 1414631 (2018).

[7] X. Wan, A. M. Turner, A. Vishwanath, and S. Y. Savrasov, Phys. Rev. B **83**, 205101 (2011).

[8] A. A. Burkov, M. D. Hook, and L. Balents, Phys. Rev. B **84**, 235126 (2011).

[9] S.-Y. Xu, C. Liu, S. K. Kushwaha, R. Sankar, J. W. Krizan, I. Belopolski, M. Neupane, G. Bian, N. Alidoust, T.-R. Chang, H.-T. Jeng, C.-Y. Huang, W.-F. Tsai, H. Lin, P. P. Shibayev, F.-C. Chou, R. J. Cava, and M. Z. Hasan, Science **347**, 294 (2015).

[10] S.-M. Huang, S.-Y. Xu, I. Belopolski, C.-C. Lee, G. Chang, B. Wang, N. Alidoust, G. Bian, M. Neupane, C. Zhang, S. Jia, A. Bansil, H. Lin, and M. Z. Hasan, Nat. Commun. **6**, 7373 (2015).

[11] Y.-H. Chan, C.-K. Chiu, M. Y. Chou, and A. P. Schnyder, Phys. Rev. B **93**, 205132 (2016).

[12] G. Bian, T.-R. Chang, R. Sankar, S.-Y. Xu, H. Zheng, T. Neupert, C.-K. Chiu, S.-M. Huang, G. Chang, I. Belopolski, D. S. Sanchez, M. Neupane, N. Alidoust, C. Liu, B. Wang, C.-C. Lee, H.-T. Jeng, C. Zhang, Z. Yuan, S. Jia, A. Bansil, F. Chou, H. Lin, and M. Z. Hasan, Nat. Commun. **7**, 10556 (2016).

[13] G. Bian, T. R. Chang, H. Zheng, S. Velury, S. Y. Xu, T. Neupert, C. K. Chiu, S. M. Huang, D. S. Sanchez, I. Belopolski, N. Alidoust, P. J. Chen, G. Chang, A. Bansil, H. T. Jeng, H. Lin, and M. Z. Hasan, Phys. Rev. B **93**, 121113(R) (2016).

[14] W. B. Rui, Y. X. Zhao, and A. P. Schnyder, Phys. Rev. B **97**, 161113(R) (2018).

[15] T. Bzdusek, Q. Wu, A. Rüegg, M. Sigrist, and A. A. Soluyanov, Nature (London) **538**, 75 (2016).

[16] Z. Shi, M. Wang, and J. Wu, Appl. Phys. Lett. **107**, 102403 (2015).

[17] J. R. Schaibley, H. Yu, G. Clark, P. Rivera, J. S. Ross, K. L. Seyler, W. Yao, and X. Xu, Nat. Rev. Mater. **1**, 16055 (2016).

[18] C.-K. Chiu and A. P. Schnyder, Phys. Rev. B **90**, 205136 (2014).

[19] K. Shiozaki and M. Sato, Phys. Rev. B **90**, 165114 (2014).

[20] Y. X. Zhao, A. P. Schnyder, and Z. D. Wang, Phys. Rev. Lett. **116**, 156402 (2016).

[21] A. H. Castro Neto, F. Guinea, N. M. R. Peres, K. S. Novoselov, and A. K. Geim, Rev. Mod. Phys. **81**, 109 (2009).

[22] Z. Wang, Y. Sun, X.-Q. Chen, C. Franchini, G. Xu, H. Weng, X. Dai, and Z. Fang, Phys. Rev. B **85**, 195320 (2012).

[23] C.-K. Chiu and A. P. Schnyder, J. Phys.: Conf. Ser. **603**, 012002 (2015).

[24] Z. Wang, H. Weng, Q. Wu, X. Dai, and Z. Fang, Phys. Rev. B **88**, 125427 (2013).

[25] L. S. Xie, L. M. Schoop, E. M. Seibel, Q. D. Gibson, W. Xie, and R. J. Cava, APL Mater. **3**, 083602 (2015).

[26] A. Yamakage, Y. Yamakawa, Y. Tanaka, and Y. Okamoto, J. Phys. Soc. Jpn. **85**, 013708 (2016).

[27] S. M. Young, S. Zaheer, J. C. Y. Teo, C. L. Kane, E. J. Mele, and A. M. Rappe, Phys. Rev. Lett. **108**, 140405 (2012).

[28] L. M. Schoop, M. N. Ali, C. Straßer, A. Topp, A. Varykhalov, D. Marchenko, V. Duppel, S. S. P. Parkin, B. V. Lotsch, and C. R. Ast, Nat. Commun. **7**, 11696 (2016).

[29] Y. X. Zhao and A. P. Schnyder, Phys. Rev. B **94**, 195109 (2016).

[30] L. Michel and J. Zak, Phys. Rev. B **59**, 5998 (1999).

[31] S. M. Young and C. L. Kane, Phys. Rev. Lett. **115**, 126803 (2015).

[32] A. Alexandradinata, Z. Wang, and B. A. Bernevig, Phys. Rev. X **6**, 021008 (2016).

[33] A. Furusaki, Sci. Bull. **62**, 788 (2017).

[34] R. Takahashi, M. Hirayama, and S. Murakami, Phys. Rev. B **96**, 155206 (2017).

[35] B.-J. Yang, T. A. Bojesen, T. Morimoto, and A. Furusaki, Phys. Rev. B **95**, 075135 (2017).

[36] S. S. Tsirkin, I. Souza, and D. Vanderbilt, Phys. Rev. B **96**, 045102 (2017).

[37] C. Fang, Y. Chen, H.-Y. Kee, and L. Fu, Phys. Rev. B **92**, 081201(R) (2015).

[38] M. Malard, P. E. de Brito, S. Ostlund, and H. Johannesson, Phys. Rev. B **98**, 165127 (2018).

[39] J. Zhang, Y.-H. Chan, C.-K. Chiu, M. G. Vergniory, L. M. Schoop, and A. P. Schnyder, Phys. Rev. Mater. **2**, 074201 (2018).

[40] R. Chen, H. C. Po, J. B. Neaton, and A. Vishwanath, Nat. Phys. **14**, 55 (2018).

[41] B. Bradlyn, L. Elcoro, J. Cano, M. G. Vergniory, Z. Wang, C. Felser, M. I. Aroyo, and B. A. Bernevig, Nature (London) **547**, 298 (2017).

[42] L. M. Schoop, A. Topp, J. Lippmann, F. Orlandi, L. Müchler, M. G. Vergniory, Y. Sun, A. W. Rost, V. Duppel, M. Krivenkov, S. Sheoran, P. Manuel, A. Varykhalov, B. Yan, R. K. Kremer, C. R. Ast, and B. V. Lotsch, Sci. Adv. **4**, eaar2317 (2018).

[43] A. Topp, J. M. Lippmann, A. Varykhalov, V. Duppel, B. V. Lotsch, C. R. Ast, and L. M. Schoop, New J. Phys. **18**, 125014 (2016).

[44] S. A. Parameswaran, A. M. Turner, D. P. Arovas, and A. Vishwanath, Nat. Phys. **9**, 299 (2013).

[45] H. Watanabe, H. C. Po, M. P. Zaletel, and A. Vishwanath, Phys. Rev. Lett. **117**, 096404 (2016).

[46] T. Zhang, Y. Jiang, Z. Song, H. Huang, Y. He, Z. Fang, H. Weng, and C. Fang, Nature (London) **566**, 475 (2019).

[47] M. G. Vergniory, L. Elcoro, C. Felser, N. Regnault, B. A. Bernevig, and Z. Wang, Nature (London) **566**, 480 (2019).

[48] F. Tang, H. C. Po, A. Vishwanath, and X. Wan, Nature (London) **566**, 486 (2019).

[49] L. Michel and J. Zak, Phys. Rep. **341**, 377 (2001).

[50] J. Kruthoff, J. de Boer, J. van Wezel, C. L. Kane, and R.-J. Slager, Phys. Rev. X **7**, 041069 (2017).

[51] L. Elcoro, B. Bradlyn, Z. Wang, M. G. Vergniory, J. Cano, C. Felser, B. A. Bernevig, D. Orobengoa, G. de la Flor, and M. I. Aroyo, J. Appl. Crystallogr. **50**, 1457 (2017).

[52] C. Bradley and A. P. Cracknell, *The Mathematical Theory of Symmetry in Solids: Representation Theory for Point Groups and Space Groups* (Clarendon Press, Oxford, 1972).

[53] S. C. Miller and W. F. Love, *Tables of Irreducible Representations of Space Groups and Co-representations of Magnetic Groups* (Pruett, Boulder, 1967).

[54] H. Nielsen and M. Ninomiya, Nucl. Phys. B **185**, 20 (1981).

[55] We note that at the A point there exist both two-dimensional and four-dimensional irreps. Hence, nodal lines are also possible in the $k_x = 0$ plane, but they are not guaranteed to exist by symmetry alone.

[56] See https://icsd.fiz-karlsruhe.de.

[57] S. Curtarolo, W. Setyawan, S. Wang, J. Xue, K. Yang, R. H. Taylor, L. J. Nelson, G. L. Hart, S. Sanvito, M. Buongiorno-Nardelli, N. Mingo, and O. Levy, Comput. Mater. Sci. **58**, 227 (2012).

[58] A. Jain, S. P. Ong, G. Hautier, W. Chen, W. D. Richards, S. Dacek, S. Cholia, D. Gunter, D. Skinner, G. Ceder, and K. A. Persson, APL Mater. **1**, 011002 (2013).

[59] Materials Project, http://www.materialsproject.org.

[60] G. Kresse and J. Furthmüller, Phys. Rev. B **54**, 11169 (1996).

[61] G. Kresse and J. Furthmüller, Comput. Mater. Sci. **6**, 15 (1996).

[62] P. E. Blöchl, Phys. Rev. B **50**, 17953 (1994).

[63] G. Kresse and D. Joubert, Phys. Rev. B **59**, 1758 (1999).

[64] J. P. Perdew, K. Burke, and M. Ernzerhof, Phys. Rev. Lett. **77**, 3865 (1996).

[65] A. D. Becke and E. R. Johnson, J. Chem. Phys. **124**, 221101 (2006).

[66] F. Tran and P. Blaha, Phys. Rev. Lett. **102**, 226401 (2009).

[67] C. L. Teske, Z. Anorg. Allg. Chem. **419**, 67 (1976).

[68] C. L. Teske, Z. Naturforsch. B **34**, 386 (1979).

[69] I. Tordjman, A. Boudjada, J.-C. Guitel, and R. Masse, Acta Crystallogr., Sect. B **34**, 3723 (1978).

[70] C. Adenis, V. Langer, and O. Lindqvist, Acta Crystallogr. Sect. C **45**, 941 (1989).

[71] N. Jaussaud, P. Toulemonde, M. Pouchard, A. San Miguel, P. Gravereau, S. Pechev, G. Goglio, and C. Cros, Solid State Sci. **6**, 401 (2004).

[72] A. A. Mostofi, J. R. Yates, Y.-S. Lee, I. Souza, D. Vanderbilt, and N. Marzari, Comput. Phys. Commun. **178**, 685 (2008).

[73] Z. Tong, J. Yuan, J. Chen, A. Wu, W. Huang, C. Han, Q. Cai, C. Ma, Y. Liu, L. Fang, and Z. Liu, Mater. Lett. **237**, 130 (2019).

[74] P. Cherin and P. Unger, Acta Crystallogr. **23**, 670 (1967).

[75] Note that depending on the chirality of these chains Te can also be in SG No. 153 ($P3_212$).

[76] M. Hirayama, R. Okugawa, S. Ishibashi, S. Murakami, and T. Miyake, Phys. Rev. Lett. **114**, 206401 (2015).

[77] K. Nakayama, M. Kuno, K. Yamauchi, S. Souma, K. Sugawara, T. Oguchi, T. Sato, and T. Takahashi, Phys. Rev. B **95**, 125204 (2017).

[78] L. A. Agapito, N. Kioussis, W. A. Goddard, and N. P. Ong, Phys. Rev. Lett. **110**, 176401 (2013).

[79] P. Cherin and P. Unger, Inorg. Chem. **6**, 1589 (1967).

[80] N. Jaussaud, M. Pouchard, P. Gravereau, S. Pechev, G. Goglio, C. Cros, A. San Miguel, and P. Toulemonde, Inorg. Chem. **44**, 2210 (2005).

[81] C. K. Chiu, Y. H. Chan, and A. P. Schnyder, arXiv:1810.04094.

[82] Note that there is only one type of termination.

[83] K. von Klitzing and G. Landwehr, Solid State Commun. **9**, 2201 (1971).

[84] L. D. Laude, R. F. Willis, and B. Fitton, Phys. Rev. Lett. **29**, 472 (1972).

[85] T. Englert, K. von Klitzing, R. Silbermann, and G. Landwehr, Phys. Status Solidi B **81**, 119 (1977).